GEOPHYSICS®

CHARACTERIZATION OF FRACTURED ZONES VIA TOPOLOGICAL ANALYSIS OF 3D SEISMIC DIFFRACTION IMAGES

Journal:	*Geophysics*
Manuscript ID	GEO-2018-0431.R3
Manuscript Type:	Technical Paper
Keywords:	diffraction, fractures, reconstruction, statistics
Area of Expertise:	Seismic Attributes and Pattern Recognition, Seismic Amplitude Interpretation

Geophysics

Characterization of fractured zones via topological analysis of 3D seismic diffraction images

M.I. Protasov[1], T.S. Khachkova[2], D.R. Kolyukhin[3], I.V. Bazaikin[4]

Right Running head: Fractures via topology of diffractions

[1]Institute of Petroleum Geology and Geophysics, Novosibirsk, Russia. Novosibirsk State University, Novosibirsk, Russia. E-mail: protasovmi@ipgg.sbras.ru.

[2]Institute of Petroleum Geology and Geophysics, Novosibirsk, Russia. E-mail: khachkovats@ipgg.sbras.ru.

[3]Institute of Petroleum Geology and Geophysics, Novosibirsk, Russia. E-mail: kolyukhindr@ipgg.sbras.ru.

[4]Institute of Mathematics, Novosibirsk, Russia. Institute of Petroleum Geology and Geophysics, Novosibirsk, Russia. E-mail: bazaikin@gmail.com

Geophysics

Abstract

A workflow for recovering fracture network characteristics from seismic data is considered. First, the presented discrete fracture modeling technique properly describes fracture models on the seismic scale. The key procedure of the workflow is 3D diffraction imaging based on the spectral decomposition of different combinations of selective images. Selective images are obtained by the prestack asymmetric migration procedure, while spectral decomposition occurs in the Fourier domain with respect to the spatial dip and the azimuth angles. At the final stage, we propose a topological analysis based on the construction of a merge tree from the obtained diffraction images. The results of the topological algorithm are modeling parameters for the discrete fractures. To analyze the effectiveness of the proposed workflow, a statistical comparison of the recovered parameters and true model parameters are provided. We use the Kolmogorov-Smirnov test for a statistical analysis of the fracture lengths, while behavior of the Morisita index shows the statistical distribution of the modeled fracture corridors. Numerical examples with synthetic realistic models demonstrate a detailed, reliable reconstruction of the statistical characteristics of the fracture corridors.

Keywords

Discrete fracture networks, 3D diffraction images, fractured zones, computational and applied topology, merge tree.

Introduction

Fractures and faults significantly affect the fluid flow in natural reservoirs. The ability to precisely locate fractures as well as characterize and model their properties is of high importance. The paper presents a combination of the techniques to recover fracture characteristics from seismic data for further modeling of reservoirs.

First, we develop a statistical model that adequately describes fracture systems on the seismic scale. The main existing approaches to statistical modeling of fracture systems are described in (Tran, 2007; Xu and Dowd, 2010). Explicit statistical modeling of fracture networks and evaluations of the medium permeability were carried out, for example, in (Odling et al. 2004; Tran and Ravoof, 2007). Here, we use the concept of a discrete fracture network (DFN) that requires an explicit spatial position, size and orientation for each fracture (Xu and Dowd, 2010). Thus, the fractures' attributes (i.e., direction and size) are defined by corresponding statistical distributions.

Various techniques have been developed to locate microstructures, i.e., fractures through the analysis of diffracted/scattered elastic waves. The paper by Fomel, Landa, and Taner (2007) introduced the application of the so-called plane wave destructor for separating scattering/diffraction and reflections. This method is especially useful for computing time stacks, or common offset gathers along with their migrated images. In this way, one develops classical images for the scattered/diffracted component of the wave-field. Moser and Howard (2008)

developed diffraction imaging in the depth domain in the context of a prestack migration. They recognized that regular migration can be implemented in two stages: the first step images the specular reflections, whereas the second suppresses and weakens the images of the specular reflections to reveal the images of diffractions. We use 3D diffraction imaging workflows for fracture detections that contain two main procedures: the prestack asymmetric migration procedure, which is a weighted data summation, and image spectral decomposition (Protasov et al., 2016, 2017, 2018). Thus, for a seismic model that contains modeled fractures, we provide this 3D diffraction imaging.

Then, to obtain the information about the fracture parameters we propose an original topological analysis of the diffraction images that contain fractured zones. Such an analysis is based on the observation that different amplitude levels of diffraction images give topologically different objects. In this situation, the information about those objects can be extracted via computational topology algorithms (Bazaikin et al., 2013). Finally, the numerical results for the generated synthetic model are presented and discussed.

Geophysics

DFN modeling: seismic scale

For the statistical modeling of a fracture system, we used the general approach described in (Xu and Dowd, 2010). Fractures are represented in the form of oblate tri-axial ellipsoids. The orientation of the ellipsoid plane is determined by the direction of the normal parallel to the smaller axis of the ellipsoid. For all the models considered, the average value of dip angle is chosen equal to pi/2, i.e., fractures are vertical. The average value of the dip direction and the variance of the deviation from this direction are selected separately for each fracture family. The geometric dimensions of the fractures are determined by the lengths of the principal axes (or semi-axes). Following (Xu and Dowd, 2010), the major axis (fracture length) L is modeled statistically. The value of the medium axis (fracture width) W is determined from the simulated fracture length L by specifying the statistical distribution L/W. The value of the minor axis (fracture thickness) T is given as a constant.

In this paper, for statistical modeling we used the normal $N(\mu, \sigma^2)$ and lognormal ln $N(\mu, \sigma^2)$ probability distributions with mean μ and variance σ^2:

$$f(x) = \frac{1}{\sigma\sqrt{2\pi}} e^{-\frac{(x-\mu)^2}{2\sigma^2}},$$

$$f(x) = \frac{1}{x\sigma\sqrt{2\pi}} e^{-\frac{(\ln x-\mu)^2}{2\sigma^2}}.$$

After modeling the geometry of the fractures, the next step is to sample the model on a coarse grid. The complexity of the problem is due to the thickness of the fractures being usually much smaller than the cell size. To overcome this issue, the

average value of the indicator function is calculated for each cell of a sparse grid using statistical modeling. Thus, finally, we obtain a fracture intensity indicator function that is computed on the chosen sparse grid. However, in this case, the question arises of what grid step can be used. To answer this question, we construct seismic images for a given frequency range for several models with different steps. Starting with a fine grid, we enlarge the step while the image remains unchanged.

The cluster model for the spatial distribution of fractures is developed for seismic scale fracture modeling. At the first stage, families of large fractures (or fracture corridors) are modeled. Next, in the vicinity of each large fracture, the centers of small fractures and the values of their geometric attributes are generated. The size of the fractured zone is 2000 m×2000 m×500 m, and the grid spacing is 1 m×1 m×1 m. The parameters that define the geometry of small and large fractures are presented in Tables 1 and 2, respectively. The general methods of statistical modeling of the random variables with these probability distributions are described, for example, in (Rubinstein, 1981). The example of the model with two families of large fractures as presented in Figure 1 is: 80 large fractures from the first family and 120 fractures from the second family. The random coordinates of the centers of large fractures were generated independently and uniformly in the computational domain.

Geophysics

Diffraction imaging: fracture localization

For the localization of fractured zones, we use the diffraction imaging technique that is based on the asymmetric migration of 3D surface seismic data proposed in the paper (Protasov et al., 2017):

$$\begin{aligned}\text{Image}(\mathbf{x};\text{az},\beta) = \int \tau_p^{gb_2}(x_s,y_s;\mathbf{x},\gamma,\theta,az,\beta;\omega)\boldsymbol{\tau}_{\text{p}}^{gb_1}(x_r,y_r;\mathbf{x},\gamma,\theta,az,\beta;\omega)\\ \mathbf{data}(x_r,y_r;x_s,y_s;\omega)k(\mathbf{x},\gamma,\theta,\beta)dx_r dy_r dx_s dy_s d\omega d\gamma d\theta\end{aligned}. \quad (1)$$

Here, $\text{Image}(\mathbf{x};\text{az},\beta)$ is the recovered function, $\mathbf{data}(x_r,y_r;x_s,y_s;\omega)$ is multicomponent surface seismic data in the frequency domain, and $\tau_{gbp}^{s}(x_s,y_s;\omega;\alpha,\theta,az,\beta)$, $\boldsymbol{\tau}_{gbp}^{r}(x_r,y_r;\omega;\alpha,\theta,az,\beta)$ are normal derivatives of Gaussian beams together with their potentials at the source positions. The beams are computed by ray tracing from every image point (see Figure 2a), and their derivatives depend on the structural dip, azimuth, and opening angles (see Figure 2b).

The left-hand side of the imaging formula (1) determines the 3D spatial Fourier transform of the unknown function $f(\mathbf{x};\text{az},\beta)$ followed by its quasi-inverse:

$$\text{Image}(\mathbf{x};\text{az},\beta) = \iiint\limits_{X_{par}(\mathbf{x})} e^{i\cdot\mathbf{p}\cdot\mathbf{x}} F(\omega(\mathbf{p}))d\bar{p} \iiint\limits_{X} e^{-i\cdot\mathbf{p}\cdot\mathbf{y}} \cdot f(\mathbf{y};az,\beta)d\mathbf{y}. \quad (2)$$

Here, $f = \lambda_1 + 2\mu_1\cos^2(2\beta) + v_0^{p^2}\rho_1\cos(2\beta)$. This is not the exact inversion of the Fourier transform because it is performed not over the whole phase space, but only over its subdomain X_{par} (the set of partial reconstruction, see Protasov et al., 2016). This subdomain is a circular sector that is defined by the frequency bandwidth [ω_1, ω_2] of the source function and the available range of structural dip and azimuth angles [α_1, α_2], [θ_1, θ_2] (see Figure 3):

$$X_{par} = \{(p_x, p_y, p_z) : \omega_1 \le \frac{\sqrt{p_x^2+p_y^2+p_z^2}\cdot c_0(\mathbf{x})}{2\cos(\beta)} \le \omega_2; \alpha_1 \le \text{atan}(\frac{\sqrt{p_x^2+p_y^2}}{p_z}) \le \alpha_2; \theta_1 \le \text{asin}(\frac{p_y}{p_x}) \le \theta_2\}. \quad (3)$$

The structure of the partial reconstruction set, defined by (3), lies at the heart of the proposed method of imaging of subseismic heterogeneities. The main principles are explained as follows: by changing opening β and the dip and azimuth angles of $[\alpha_1, \alpha_2]$, $[\theta_1, \theta_2]$, respectively, one changes the structure of the set of partial reconstruction and, thus, controls the geometry of visible and invisible elements of the geological cross-section. Specifically, any small scale (subseismic) object such as a diffractor/scatterer, crack, fault, pinch, and so on, possesses an extended spatial spectrum and, thus, will be presented for a wide range of partial reconstruction sets. In contrast, any regular interface possesses a very narrow spatial spectrum and, thus, one can easily choose the geometry of the Gaussian beams that provide the partial reconstruction set without this spectrum (Protasov et al., 2017, 2018)**.**

Diffraction images are presented in Figures 4 and 5. They were created for the opening angle $\beta = 0^0$ and the range of dip angles $[\alpha_1, \alpha_2] = [10^0\ 50^0]$ but have a different range of azimuth angles: $[\theta_1, \theta_2] = [0^0\ 360^0]$ (Figure 4b), $[\theta_1, \theta_2] = [-30^0\ 60^0]$ and $[150^0\ 240^0]$ (Figure 5a), $[\theta_1, \theta_2] = [60^0\ 150^0]$ and $[240^0\ 330^0]$ (Figure 5b).

Image processing: fracture characterization

The amplitude field of the diffraction image is defined by the function $\boldsymbol{f}:\boldsymbol{U}\rightarrow\mathbb{R}$, where $\boldsymbol{U}$ is a 3D area where the diffraction image was computed. We define the number $\boldsymbol{n}$ to be a discretization level of the values of the function $\boldsymbol{f}$. We define values $\boldsymbol{a_i = v_{min} + i\frac{v_{max}-v_{min}}{n}}$, $\boldsymbol{i = 0,...,n}$, where $\boldsymbol{v_{min}}$ and $\boldsymbol{v_{max}}$ are minimum and

maximum values of the function $\boldsymbol{f}$. Then, we consider the family of excursion sets $\boldsymbol{M_i} = \{(\boldsymbol{x},\boldsymbol{y},\boldsymbol{z}) \,|\, \boldsymbol{f}(\boldsymbol{x},\boldsymbol{y},\boldsymbol{z}) \leq \boldsymbol{a_i}\}$, $\boldsymbol{i} = \boldsymbol{0},...,\boldsymbol{n}$. Obviously, the excursion sets are nested inside each other: $\boldsymbol{M_0} \subset \boldsymbol{M_1} \subset ... \subset \boldsymbol{M_n}$. Therefore, we can construct the merge tree $\boldsymbol{\Gamma} = \boldsymbol{\Gamma}(\boldsymbol{f})$ (for more details and more general concept overview see Appendix A and the publications: Bazaikin et al., 2013; H. Edelsbrunner, D. Letscher and A. Zomorodian, 2002; Edelsbrunner, H and Harer, J., 2010; Verri, et al., 1993; Zomorodian, Afra and Carlsson, Gunnar, 2005).

The geometric characteristics of each connected component of each excursion set are stored in the fields of the corresponding vertex of the merge tree $\boldsymbol{\Gamma}$. We postulate that the leaves of the tree $\boldsymbol{\Gamma}$ correspond to the original fractures or set of fractures. To calculate the geometric characteristics of the fracture (or fractures set) corresponding to the leaf $\boldsymbol{u}$, we find its support vertex $\boldsymbol{v}$ (the definition of support vertex is in Appendix A). Then, the characteristics of the vertex $\boldsymbol{v}$ will be the characteristics of the corresponding fracture. Assuming approximately that the fractures (or set of fractures) have an ellipsoidal form, we determine its characteristics.

The excursion sets and the corresponding merge tree are presented in Figure 6. The color of the vertex of the merge tree (Figure 6b) corresponds to the color of the amplitude field of the diffraction image (Figure 6a). On the image, three objects that are clearly defined by three branches of the corresponding merge tree can be observed.

The described algorithm was applied to the diffraction images presented above (Figures 4, 5). We provide a comparison of the original model with 2 families of large fractures (Figure 7a) and the constructed models (Figures 7b, 8a, 8b) using fracture characteristics recovered from the corresponded diffraction images (Figures 4b, 5a, 5b) by the described topological algorithm. A bad fracture reconstruction for the full diffraction image can be observed. In this case, we have an intersection of fractures from different families. In such a situation, intersected fractures can be topologically equivalent to one fracture. Therefore, we need to separate fracture families first. Then, we can observe whether the fracture families are differentiated on the images, and then the topological algorithm recovers characteristics that produce a similar picture. Moreover, most of these characteristics are statistically equivalent to the characteristics of the original model (see Table 3).

Specifically, we compare the spatial distribution of fracture centers, which was uniform for the original model. Morisita index I (Cressie, 1991) was developed to measure the variability between different subregions of the simulation domain and check the presence of cluster structures. The Morisita index is calculated for an area divided into rectangular cells of equal size using the formula:

$$I = Q\frac{\sum_{i=1}^{Q} n_i\left(n_i - 1\right)}{N\left(N-1\right)},$$

where N is the total number of fractures; Q is the number of splitting cells; n_i (i = 1, 2, ..., Q) - the number of centers in the i-th cell.

A Morisita diagram is a graph of the dependence of Morisita index I with respect to the cell size. Morisita diagrams were calculated to analyze the behavior of the distribution. The Morisita index characterizes the probability of two randomly selected points being in the same cell. There are three types of characteristic behavior with this dependence that allow for judging the distribution of the fracture centers (Savelieva, Demyanov, 2010):

• With increasing cell size, I tends to 1. Then, the distribution of points can be considered uniform.

• The value of I does not depend on the size of the cell and is approximately equal to ≈ 1 (fluctuates approximately 1). This means that the distribution of points is random and does not have cluster structures.

• With increasing cell size, I decreases or grows above 1 — the distribution of network points is clustered.

The first condition is satisfied for all the cases considered. Table 3 shows the magnitude (index I tends to that magnitude).

The number of the recovered fracture corridors is less than the number of fracture corridors in the model. This means that the recovery is not perfect. However, the behavior of the Morisita index shows that the statistical distribution of the modeled and recovered fracture corridors and are very close for both families. Additionally, the other parameters, i.e., the average length values and average direction values of the modeled and recovered fracture corridors are very close.

Since the amplitude function is specified with some distortions in practice, the set of excursions contains the connected components provided by local oscillations of the function $\boldsymbol{f}$. As a result, the merge tree contains additional branches that can distort the results of the algorithm. To avoid such distortions, we consider the critical level of the volume $\boldsymbol{V_0}$(noise level) of the connected component and leave in the constructed tree $\boldsymbol{\Gamma}$ only those vertices $\boldsymbol{u}$ that satisfy the inequality $\boldsymbol{V(u) \leq V_0}$. A practical choice of the noise level is individual for every situation. Thus, our solution is to analyze the function that is several fractures recovered for the noise level (the example of such a function is presented in Figure 9). The practical rule is to take minimum noise level value where the function becomes "flat" and the number of fractures is still reasonable.

Realistic model case study

Next, we present the results for a realistic model (Landa, Reshetova Tcheverda, 2013) with a 10 km by 6 km size in the horizontal plane and 1300 meters in depth. The model contains two typical objects: a fractured collector located at depths of 1000 meters to 1200 meters (see Figure 10d, 10b) and a set of channels distributed over the entire length of the model (see Figure 10a, 10b, 10c). These objects produce scattering waves, and these are the objects of diffraction imaging. Here, we concentrate our attention on the fractured zones, which consist of fracture corridors that are our main focus for detection and characterization. Specialists generated this fractured (fracture corridors) reservoir model using a huge number of core samples

(Petit et al., 2002). Seismic data for this model were generated by finite-difference modeling with local time-space grid refinement (Kostin et al., 2015) where the source function was a Ricker pulse with a dominant frequency of 25 Hz. Here, we used zero-offset data only. Therefore, the number of sources equals the number of receivers and is equal to 569961 = 581 (x coordinate) * 981 (in y coordinate). Zero offset z-component seismograms are shown in Figure 11a) along the line y = 3100 m; b) along the cross-line x = 5100 meters. Reflected energy can mainly be observed; however, some strong diffraction events can be seen as well.

Synthetic data generated for the model were used to construct the diffraction image. The diffraction image was calculated as the sum of selective images for the dip angles that are close to 30 degrees ([25 °: 5 °: 35 °]) and for all azimuths. The opening angle β is set to zero because the synthetic data are zero offset. In this case, all the reflectors remain outside the set of partial reconstruction (see Figure 12), so the resulting image only gives the diffraction objects. Figure 12b shows the vertical sections of the diffraction image in the y = 5100 plane, and Figure 12a shows the corresponding section of the model. The images provide a relatively detailed description of the diffraction objects in the area of the buried channels. Moreover, in the vertical section (perpendicular to the fracture direction, Figure 12b) diffraction objects are visible in the region of the fracture zone.

Figure 13a presents a horizontal plane of the model containing the fractured zone, Figure 13b shows the same plane of the diffraction image. The diffraction image indicates the presence of heterogeneities and provides a detailed and well

resolved picture of them. Although the diffraction image does not describe every crack of the model (which is natural in the seismic frequency band, the dominant frequency of the signal 25 Hertz), it is close to the picture of the model itself in the fractured zone and gives a reasonably accurate fracture distribution.

To provide a comparison of the model parameters and the results of the topology analysis of the diffraction image, we extracted the discrete fracture modeling parameters from the original model. Their visualization in the fractured zone is shown in Figure 14a. Then, the topological algorithm was applied to the diffraction image inside the detected fractured area (Figure 12b, 13b). The visualization of the recovered DFN parameters from the diffraction image is shown in Figure 14b. Visually, they are rather similar to the parameters extracted from the original model. To be more precise, we provide a numerical comparison of the characteristics of the parameters of the original model and the diffraction image by statistical methods.

First, we apply the two-sample Kolmogorov-Smirnov test for a statistical analysis of the fracture lengths (the size of largest axis). This test allows for testing the null hypothesis, where the fracture lengths of the model and the diffraction image being sampled from one continuous distribution is confirmed if the p-value> 0.05. A P-value is the probability that a random variable with a given distribution (distribution of test statistics for the null hypothesis) will take a value not less than the actual value of the test statistics. Thus, for the described case P-value=0.373, this means the fracture centers of the model and the diffraction image are sampled from

one continuous distribution. Additionally, a similar behavior is observed in the distribution functions estimated for the diffraction image and original model (Figure 15a).

In this realistic case study, we did not model the distribution of fracture centers, but we did extract them from the model. Therefore, the Morisita diagrams were estimated not only for the diffraction image but also for the original model (see Figure 15b). The distribution of points has no cluster structures and is uniform for both the original model and diffraction image.

The number of the recovered fracture corridors is less than the number of fracture corridors in the model (similar to the example with the DFN model described above). This means that the recovery is not identical, but again the behavior of Morisita index shows that the statistical distributions of the model fractures and the fractures recovered from the diffraction image are very close. As previously mentioned, our main interest is the behavior of the Morisita index with the increase in epsilon (cell size). The estimation of the index for small epsilon values has a much higher uncertainty. In our case, this difference is due to the different number of fractures for the original model and diffraction image. Of course, if we increase the frequency, we will get closer results for the original model and diffraction image. Specifically, the consistency of the Morisita diagrams for the original model and images will improve with increasing frequency.

Additionally, the other parameters, i.e., average length values and average direction values of the model fractures and recovered fractures, are very close (Table 4).

Conclusions and discussion

A methodology for reconstructing discrete fracture modeling parameters by using diffraction imaging and following a topological analysis of the diffraction images is proposed in this paper. The imaging procedure outlined in this paper provides a 3D diffraction image. The main part of the algorithm is the asymmetric summation, which provides selective images and is implemented by the double focusing of Gaussian beams. The topological algorithm is based on the construction and analysis of the merge tree. A method for statistical modeling of the discrete fracture network on a seismic scale is presented. The numerical example for the realistic synthetic model shows that the diffraction images provide the detailed, reliable reconstruction of the fractured zones. The results of the topological analysis of the diffraction images for the methodological example and realistic example provide an appropriate reconstruction of the statistical distribution of the large fractures (fracture corridors), an average value of the fracture corridors' lengths and an average value of the large fractures' (fracture corridors) directions. The uniform spatial distribution of large fracture (fracture corridors) centers is also restored quite thoroughly in the seismic frequency range.

As shown in this paper, a high quality diffraction image produces a reliable reconstruction of fracture parameters within the proposed workflow. That means that for the successful application of the proposed workflow for real data, one must obtain a diffraction image of sufficient quality. We believe that this is a primary challenge in this workflow. However, the proposed diffraction imaging algorithm provides reliable diffraction images with a high signal-to-noise ratio. That means the proposed workflow will potentially provide robust results for real data.

Acknowledgements

The research described in this publication was supported by RFBR grant 17-05-00001 and by Russian Academy of Sciences within the scope of the project No. 0331-2019-0008. Yaroslav Bazaikin was supported by the Program of Fundamental Scientific Research of the SB RAS No. I.1.2., project No. 0314-2019-0006.

Appendix A: Fundamentals of computational topology: merge tree.

In this section, we present basic definitions and concepts of computational topology that we used in this article. For more details and more general concepts, we refer to [Edelsbrunner, H and Harer, J., 2010].

For subset X of Euclidean space $\mathbb{R}^3$, we state that two points $p,q \in X$ are *connected* in X if and only if continuous curve γ:$[0;1]\rightarrow X$ exists, so that $\gamma(0) = p, \gamma(1) = q$. If any two points in X are connected, we state that X is a (linear) *connected set* (we will omit the word "linear" from here). Obviously, the property of being connected is the equivalence relation for points in X and divides X into many pairwise and not intersecting connected sets X_α with the property $\cup_\alpha X_\alpha = X$. We say that X_α is the *connected components* of X. We will assume further that all sets have only a finite number connected components (it is not restrictive for our purposes because it is true for sets that are unions of unit voxels). We denote $C(X)$ to be a set of connected components. With our assumptions, $C(X)$ consists of a finite number of points where each point corresponds to a unique connected component of X. Now, we consider two subsets: $X \subset Y \subset \mathbb{R}^3$. Our definitions thus show that connected points in X are also connected in Y. This implies that there is a correct map i:$C(X)\rightarrow C(Y)$. Remark that map i, in general, is neither injective nor surjective.

Let K be a rectangle domain in Euclidean space $\mathbb{R}^3$ and consider a chain of strictly embedded sets (such chain is called *filtration* in topology):

$$X_0 \subset X_1 \subset ... \subset X_n = K.$$

Then, for every k, $0 \leq k \leq n-1$ we have a map defined as above: i_k:$C(X_k)$→$C($ X_{k+1}). Now consider the graph $\Gamma = (V,E)$, putting:

$$V = \cup_{k=0}^{n} C(X_k), E = \{(u,v) | u \in C(X_k),\ v = i_k(u) \in C(X_{k+1}),\ k = 0,...,n-1\}.$$

In other words, all connected components of X_k form vertices of Γ and every directed edge correspond to a mapping of some connected component to the higher level component. We state that vertex $u \in C(X_k)$ has (or lies on) level k. The acyclic connected graph is called a tree.

Proposition. The g*raph Γ is the tree.*

The tree Γ is called a *merge tree* corresponding to filtration $X_0 \subset ... \subset X_n$. For every edge (u,v) so that $v = i_k(u)$ for , we put the vertex u to be a child of v and vertex v to be a parent of u. Then, Γ is a directed tree with the root coinciding with the unique element in $C(K) = C(X_n)$. A vertex that has no children is called a leaf. For every leaf, $u \in C(X_k)$ consider the minimal natural l so that $i_{k+l} \circ i_{k+l-1} \circ ... \circ i_k$ (u) has more than one child. Then, we say that vertex $w = i_{k+l-1} \circ ... \circ i_k(u)$ is supporting vertex for u. This means that the connected component w is a maximal

connected component that contains u and has a unique component on every level between u and w. The supporting vertex merges with another vertex on the next level, and this is the reason why it carries the most representative geometric properties of leaf u in our approach.

References

Bazaikin, Ya.V., V.A. Baikov, I.A. Taimanov, and A.A. Yakovlev, 2013, Numerical analysis of topological characteristics of three-dimensional geological models of oil and gas fields: Math. Models and Computer Simulations, **25**, 19-31.

Cressie, N. A. C., 1991, Statistics for spatial data: John Wiley & Sons.

Edelsbrunner, H., D. Letscher and A. Zomorodian, 2002, Topological persistence and simplification: Discrete Comput. Geom., **28**, 511-533.

Edelsbrunner, H., and J. Harer, 2010, Computational Topology: An Introduction: Amer. Math. Soc.

Fomel, S., E. Landa, and T. Taner, 2007, Poststack velocity analysis by separation and imaging of seismic diffractions: Geophysics, **72**, 89-94.

Kostin, V.I., V.V. Lisitsa, G.V. Reshetova, and V.A. Tcheverda, 2015, Local time-space mesh refinement for simulation of elastic wave propagation in multi-scale media: Journal of Computational Physics, **281**, 669–689.

Landa, E., G. Reshetova, and V. Tcheverda, 2013, Exploding reflectors revisited: 3D heterogeneous multiscale elastic media: 83rd Annual International Meeting, SEG, Expanded Abstracts, 3490-3494.

Long, J. C. S., J. S. Remer, C. R. Wilson, and P. A. Witherspoon, 1982, Porous Media Equivalents for Networks of Discontinuous Fractures: Water resources research, **18**, 645-658.

Moser, T.J., and C.B. Howard, 2008, Diffraction imaging in depth: Geophysical Prospecting, **56**, 627-642.

Odling, N.E., S.D. Harris, and R.J. Knipe, 2004, Permeability scaling properties of fault damage zones in siliclastic rocks: Journal of Structural Geology, **26**, 1727-1747.

Petit, J. P., L. Bazalgette, C. Bordarier, S. Bouissou, A. Chemenda, P. Connolly, P. Cortes, C. Jorand, and G. De Joussineau, 2002, Fracture Corridors: What are They?: Inaugural Meeting of SFERA, Abstracts volume.

Protasov, M.I., G.V. Reshetova, and V.A. Tcheverda, 2016, Fracture detection by Gaussian beam imaging of seismic data and image spectrum analysis: Geophysical Prospecting, **64**, 68–82.

Protasov, M.I., G.V. Reshetova, and V.A. Tcheverda, 2017, 3D diffraction imaging of 3D seismic data via asymmetric summation and spectral filtering: Geofizika, **2**, 14-21.

Protasov, M., K. Gadylshin, V. Tcheverda, N. Isakov, and A. Pravduhin, 2018, Diffraction imaging in 3D via image spectral decomposition of partial images: Conference and Exhibition, EAGE, Expanded Abstracts, TuA01.

Rubinstein, R.Y., 1981, Simulation and the Monte Carlo method: Wiley.

Savelieva, E.A., and V.V. Demyanov, 2010, Geostatistic: theory and practice: Nauka.

Tran, N.H., 2007, Simulated annealing technique in discrete fracture network inversion: optimizing the optimization: Computational Geosciences, **11**, 249–260.

Tran, N.H., and A. Ravoof, 2007, Coupled fluid flow through discrete fracture network: A novel approach Article in International: Journal of Mathematics and Computers in Simulation, **3**, 295-299.

Verri, A., C. Uras, P. Frosini, and M. Ferri, 1993, On the use of size functions for shape analysis: Biological Cybernetics, **70**, 99–107.

Xu, C., and P. Dowd, 2010, A new computer code for discrete fracture network modeling: Computers & Geosciences, **36**, 292–301.

Zomorodian, A., and G. Carlsson, 2005, Computing Persistent Homology: Discrete & Computational Geometry, **33**, 249–274.

Figure captions.

Figure 1. Fracture intensity indicator function after DFN modeling: a - XZ plane; b - YZ plane; c – XY plane, Z=2750 m.

Figure 2. a) The geometry of the imaging method. b) The structural angles.

Figure 3. The set of partial reconstruction.

Figure 4. DFN seismic model (a) and diffraction image (b) in the XY plane (Z=2500 m).

Figure 5. Diffraction images in the XY plane (Z=2500 m): a – sum of selective images for the sector of azimuth angles [-30, 60] and [150, 240]; b – the sum of selective images for the sector of azimuth angles [60, 150] and [240, 330].

Figure 6. Image of excursion sets defined in the two-dimensional region, function growth from white to black (a); corresponding merge tree (b).

Figure 7. DFN seismic models in the XY plane (Z=2500 m): (a) the original (b) recovered from the diffraction image with all azimuth angles.

Figure 8. DFN seismic models in the XY plane (Z=2500 m) recovered from the diffraction images that are: (a) sum of selective images for sector of azimuth angles [-30, 60] and [150, 240]; (b) sum of selective images for sector of azimuth angles [60, 150] and [240, 330].

Figure 9. The function of the number of leaves of the merge tree depending on the chosen critical volume level.

Figure 10. Realistic model containing channels and a fracture zone: a) general 3D view, b) P-velocity section in the vertical plane y = 5100 m, c) P-velocity section in the vertical plane x = 3100 m, d) P-velocity section in the horizontal plane z = 1100 m.

Figure 11. Zero offset seismogram y=3100 m – (a), zero offset seismogram x=5100 m – (b).

Figure 12. The vertical section y=5100: a) – model, b) – the diffraction image.

Figure 13. The horizontal section at the level of fractured zone z=1100 m: a) – model; b) – the diffraction image.

Figure 14. DFN seismic models in the XY plane (Z=1100 m): a) – reconstructed from the model; b) – recovered from the diffraction image by topological analysis.

Figure 15. a) Empirical distribution functions estimated for the diffraction image and original model. b) Morisita diagrams estimated for the diffraction image and original model.

Table captions.

Table 1. Modeling parameters. Large fractures (fracture corridors).

Table 2. Modeling parameters. Small fractures (fracture).

Table 3. The modeled fracture characteristics and recovered fracture characteristics from the diffraction images.

Table 4. The real model fracture characteristics and fracture characteristics recovered from the diffraction images.

	1st fracture family	2nd fracture family
Density (number/m^3)	4E-8	6E-8
L (м), $N(\mu,\sigma^2)$	1000, 250	400, 100
L/W, $N(\mu,\sigma^2)$	20, 1	10, 0.5
T (м)	0.1	0.1
Orientation φ (°), $N(\mu,\sigma^2)$	90, 5	30, 10

Table 1. Modeling parameters. Large fractures (fracture corridors).

	1st fracture family	2nd fracture family
Density (number/m^3)	4E-3	6E-3
L (м), $ln\ N(\mu,\sigma^2)$	8, 2	6, 1.5
L/W, $N(\mu,\sigma^2)$	4, 0.75	3, 0.5
T (м)	0.002	0.002
Orientation φ (°), $N(\mu,\sigma^2)$	30, 5	60, 10

Table 2. Modeling parameters. Small fractures (fracture).

	Average length	Morisita Index	The average direction of the main axis	Number of fractures
DFN model family 1	401.33	0.9356	(0.8669, 0.4984, -0.0008)	120
Recovered from diffraction image Fig. 2d)	405		(0.8673, 0.4978, -0.0048)	83
DFN model family 2	1000.4	1.0078	(0.0030, 1.0000, 0.0046)	80
Recovered from diffraction image Fig. 2c)	890		(0.0070, 1.0000, -0.0018)	56

Table 3. The modeled fracture characteristics and recovered fracture characteristics from the diffraction images.

	Average length	Morisita Index	The average direction of the main axis	Number of fractures
Model	35.985	1.055	(0.0000, 0.9999, 0.0130)	144
Image	35.888	1.0	(0.0831, 0.9960, 0.0342)	48

Table 4. The real model fracture characteristics and fracture characteristics recovered from the diffraction images.

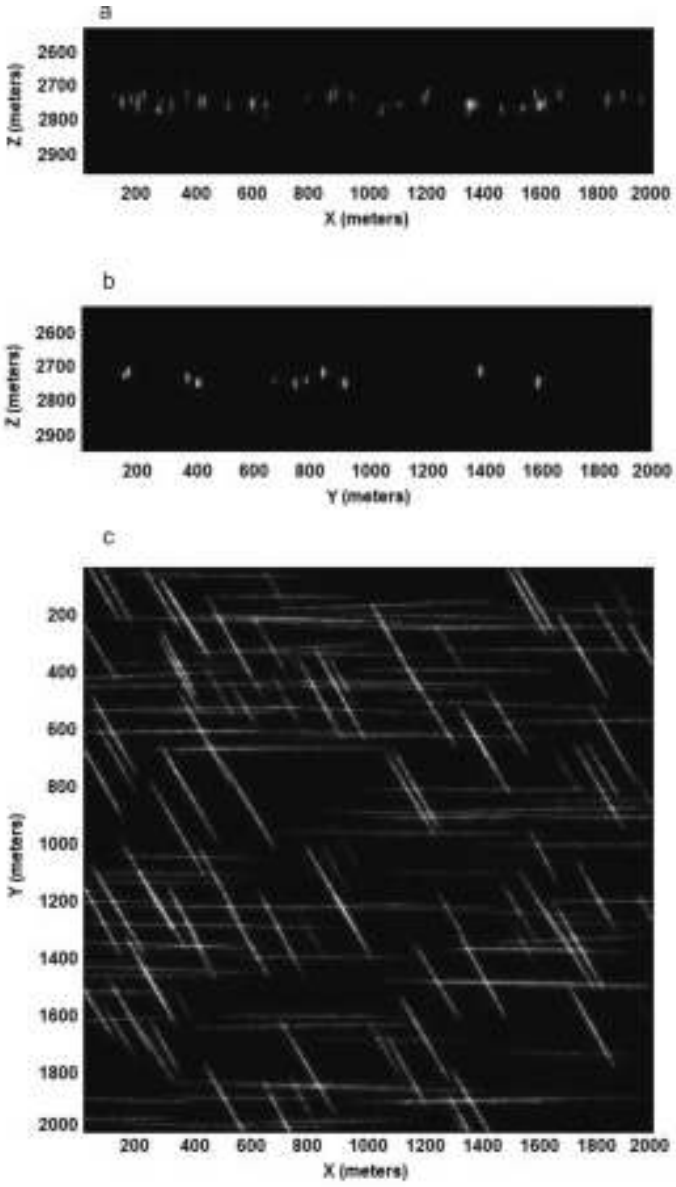

Figure 1. Fracture intensity indicator function after DFN modeling: a - XZ plane; b - YZ plane; c – XY plane, Z=2750 m.

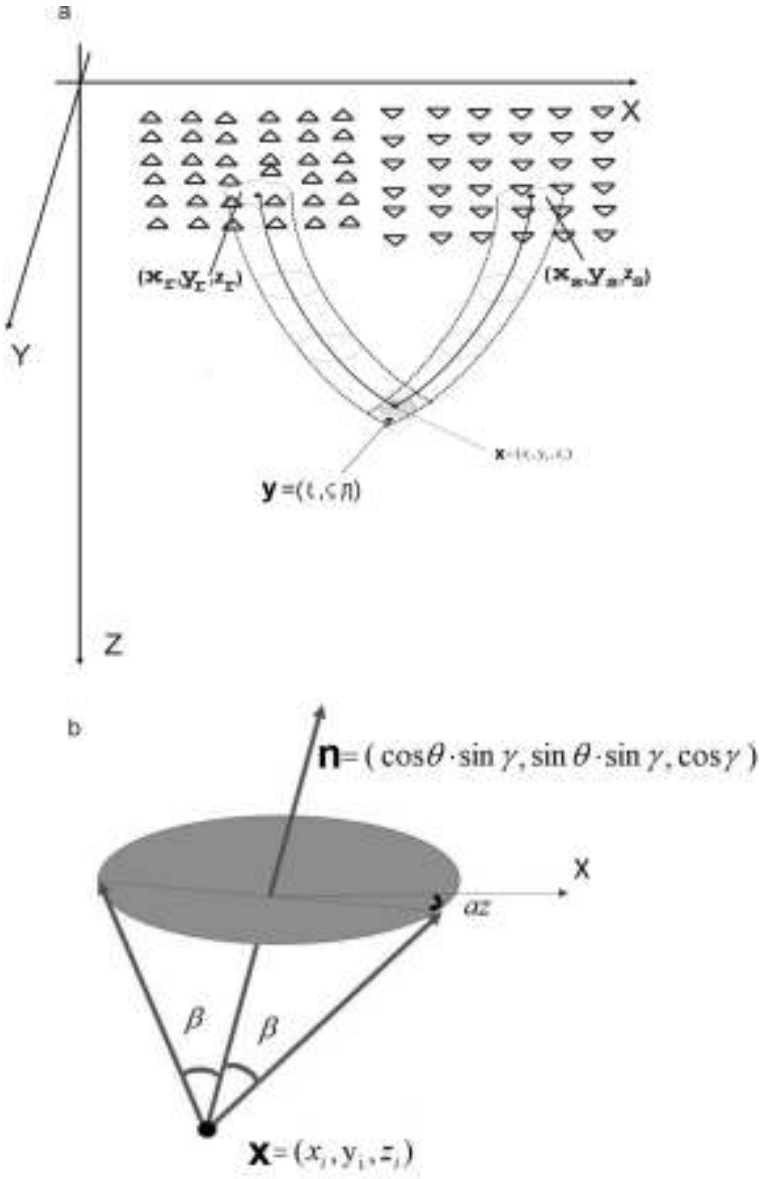

Figure 2. a) The geometry of the imaging method. b) The structural angles.

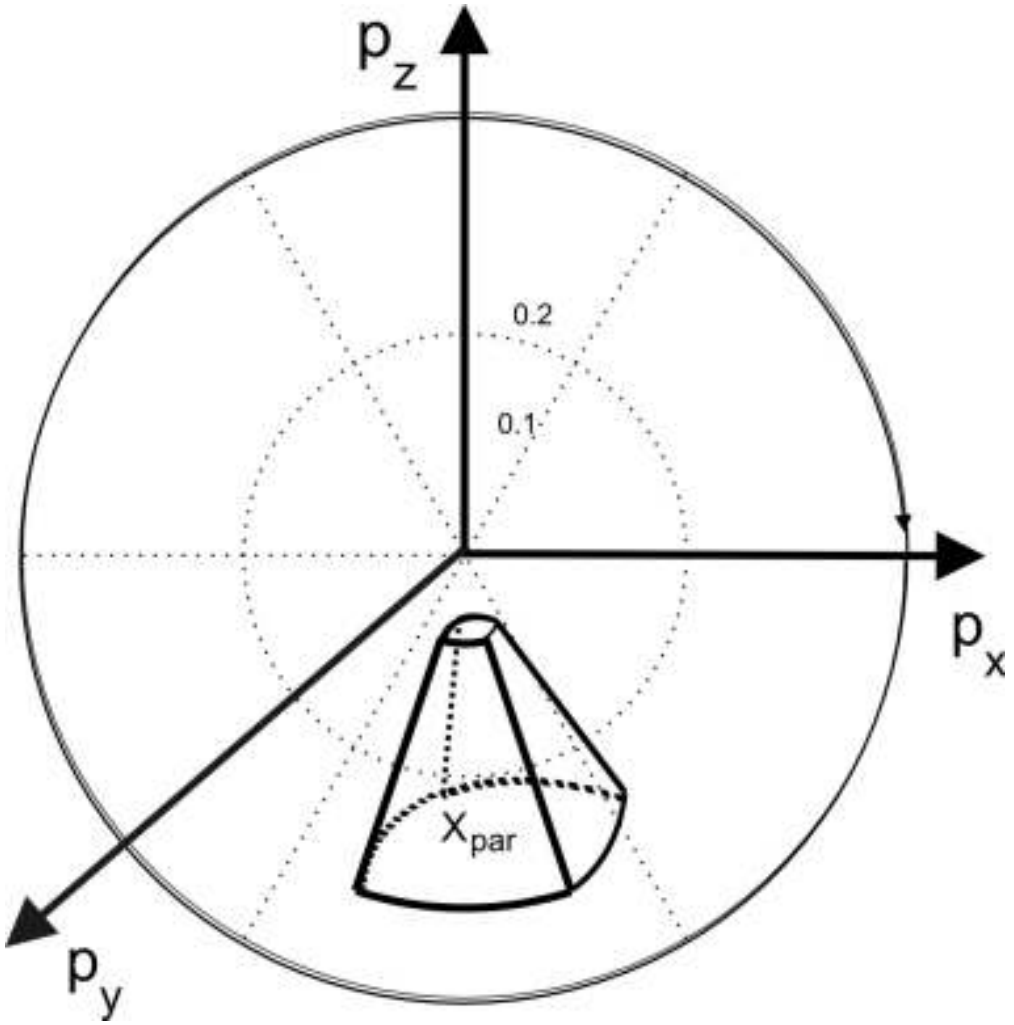

Figure 3. The set of partial reconstruction.

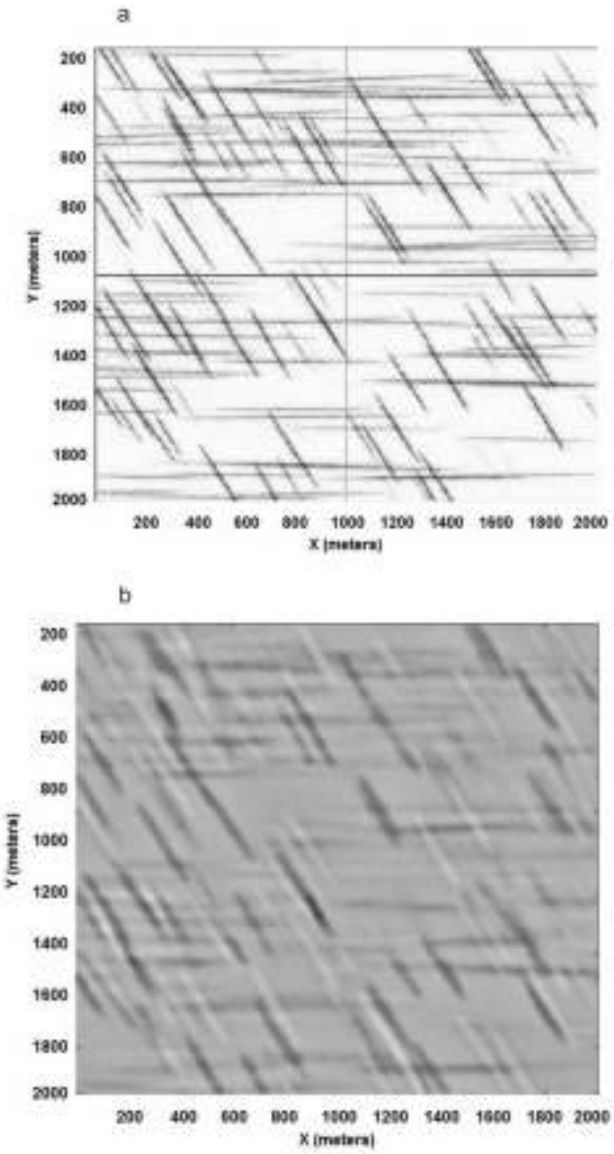

Figure 4. DFN seismic model (a) and diffraction image (b) in the XY plane (Z=2500 m).

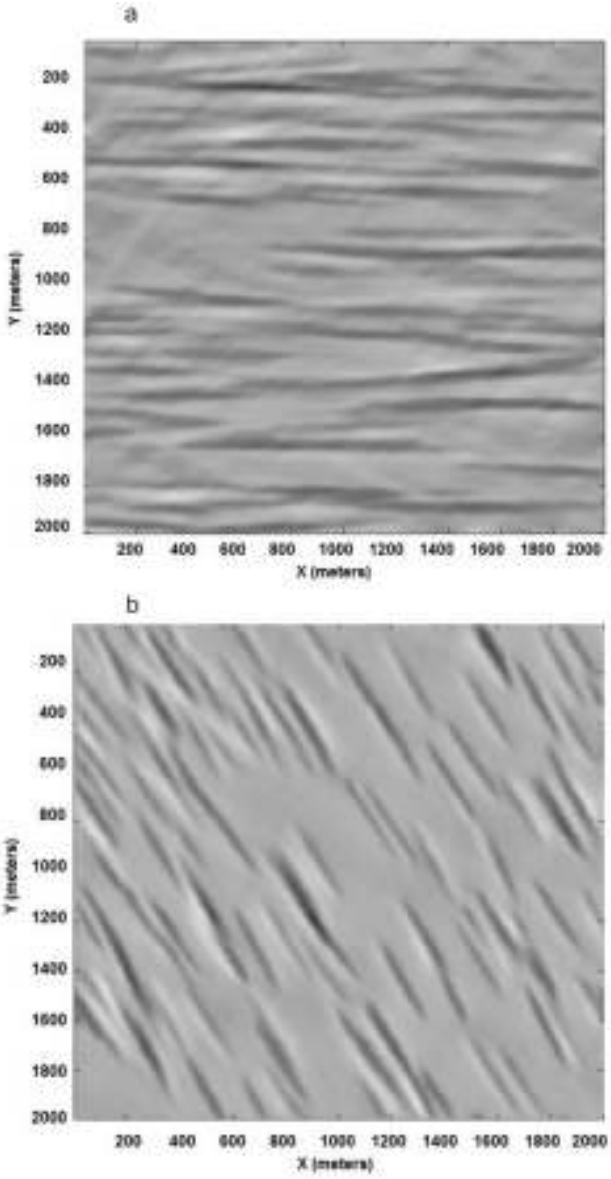

Figure 5. Diffraction images in the XY plane (Z=2500 m): a – sum of selective images for the sector of azimuth angles [-30, 60] and [150, 240]; b – the sum of selective images for the sector of azimuth angles [60, 150] and [240, 330].

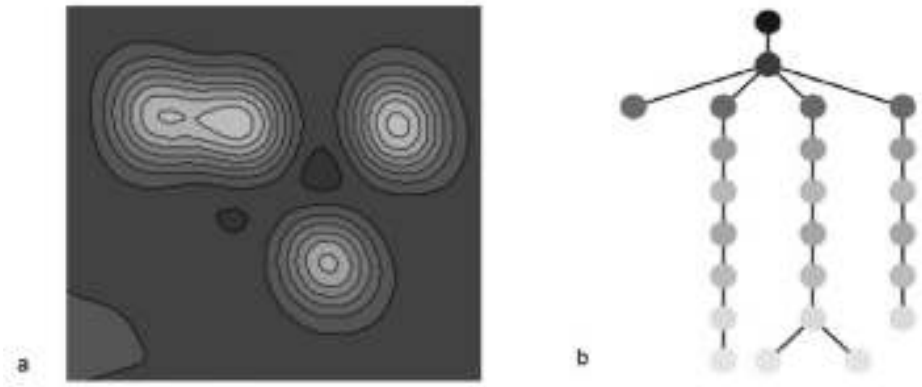

Figure 6. Image of excursion sets defined in the two-dimensional region, function growth from white to black (a); corresponding merge tree (b).

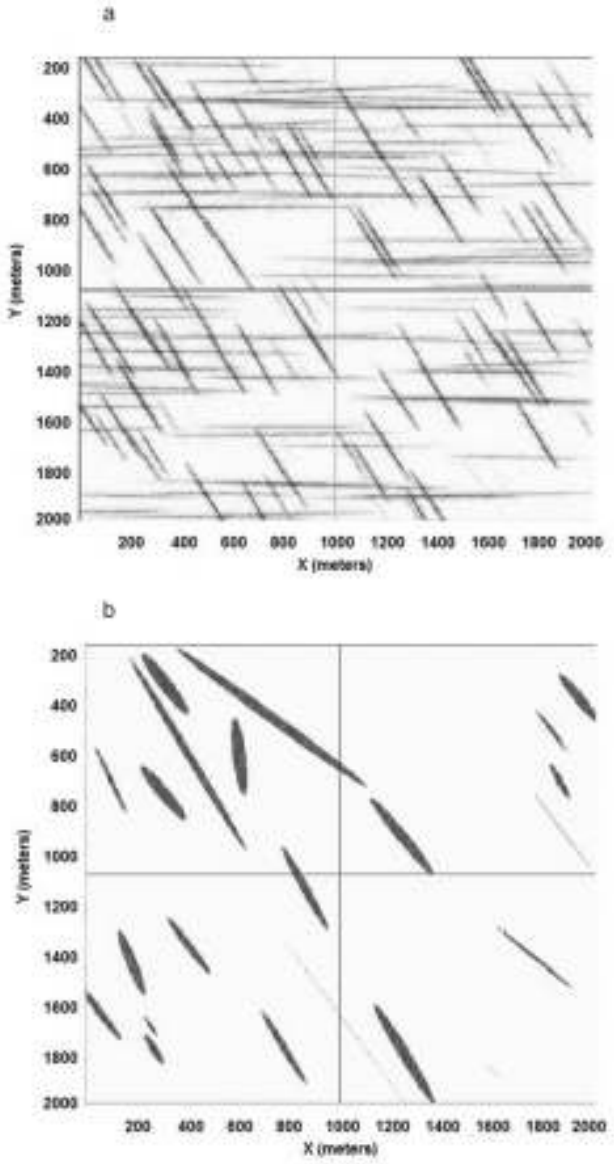

Figure 7. DFN seismic models in the XY plane (Z=2500 m): (a) the original (b) recovered from the diffraction image with all azimuth angles.

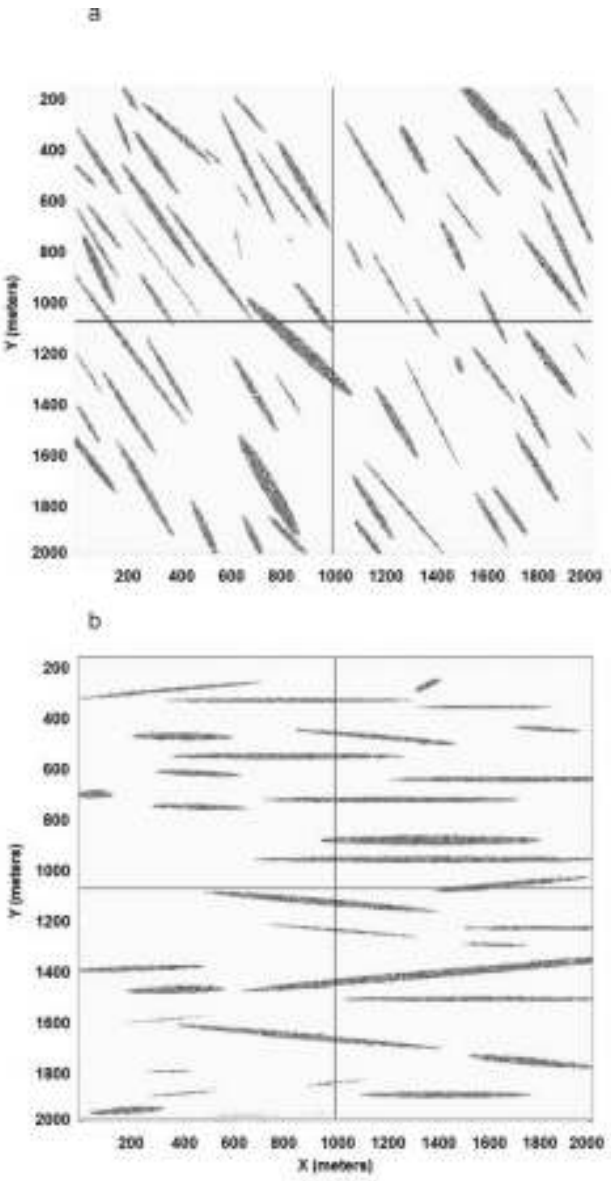

Figure 8. DFN seismic models in the XY plane (Z=2500 m) recovered from the diffraction images that are: (a) sum of selective images for sector of azimuth angles [-30, 60] and [150, 240]; (b) sum of selective images for sector of azimuth angles [60, 150] and [240, 330].

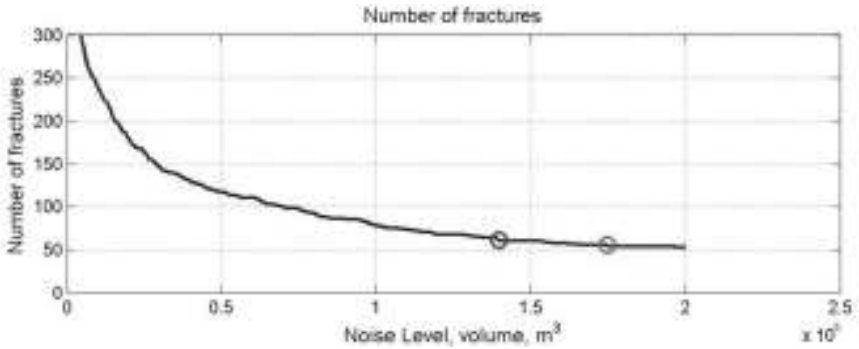

Figure 9. The function of the number of leaves of the merge tree depending on the chosen critical volume level.

204x70mm (300 x 300 DPI)

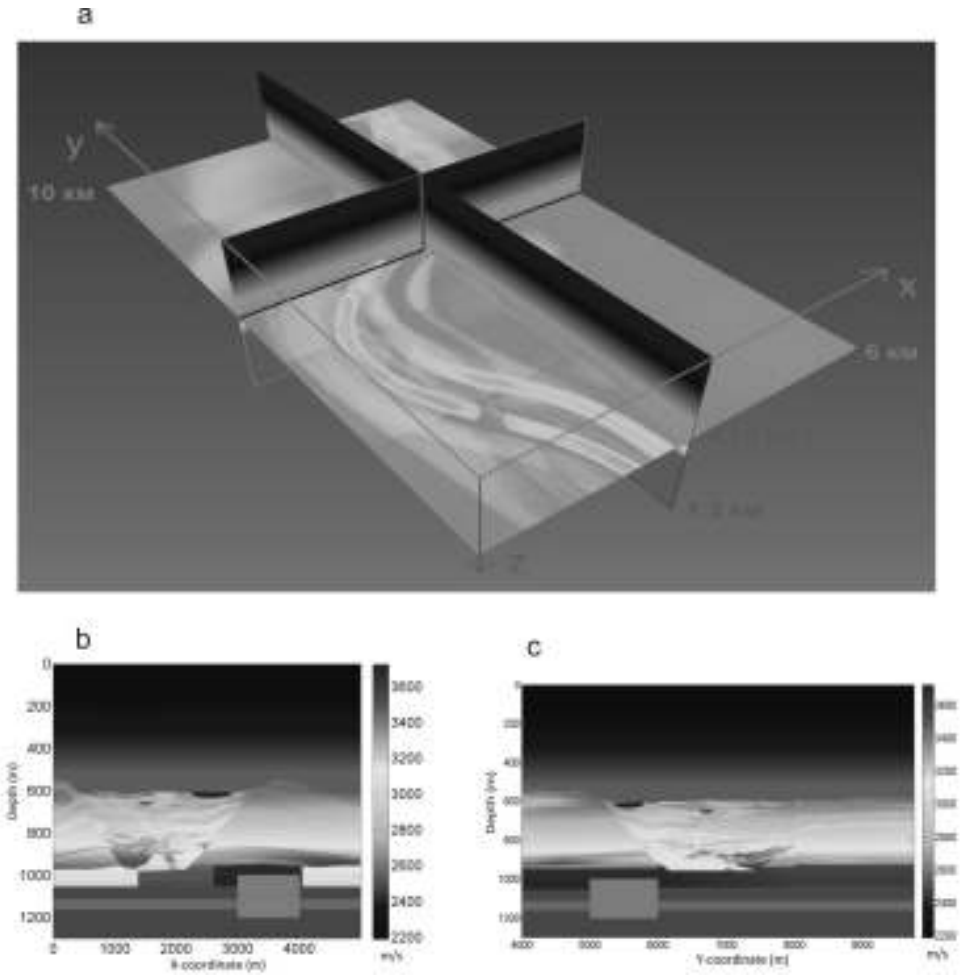

Figure 10. Realistic model containing channels and a fracture zone: a) general 3D view, b) P-velocity section in the vertical plane y = 5100 m, c) P-velocity section in the vertical plane x = 3100 m, d) P-velocity section in the horizontal plane z = 1100 m.

196x190mm (300 x 300 DPI)

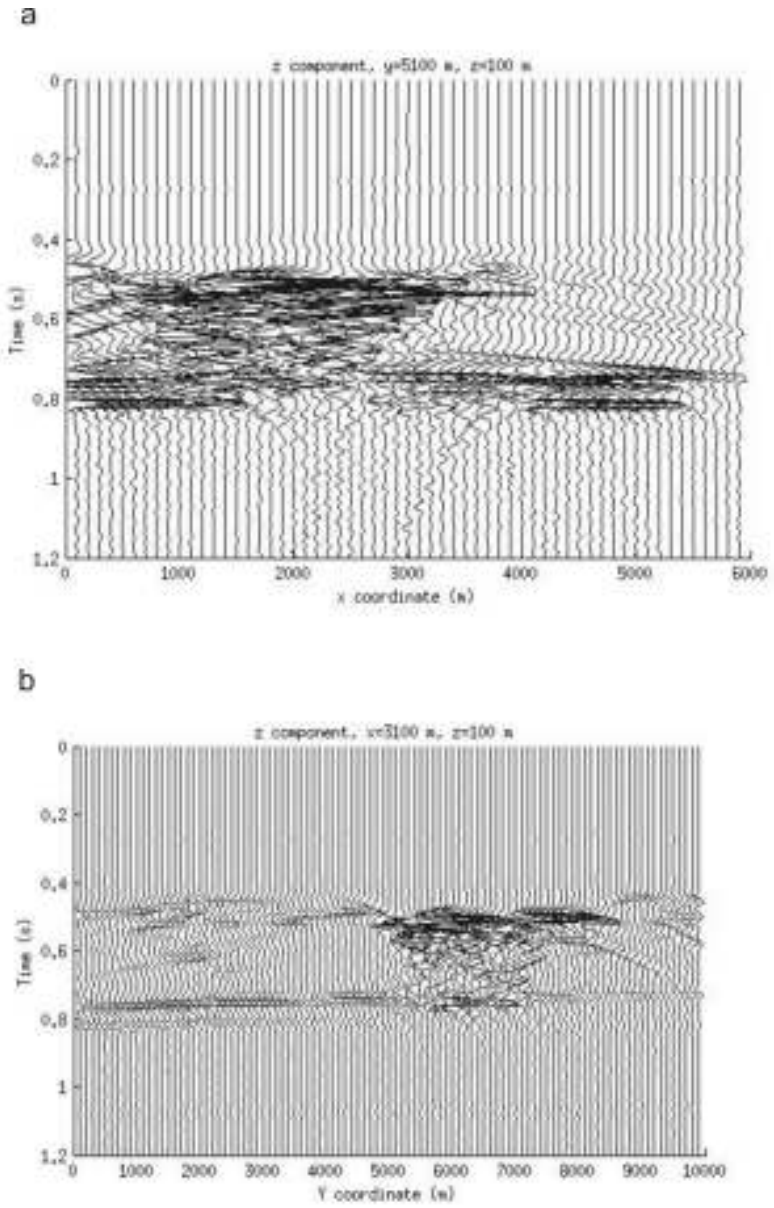

Figure 11. Zero offset seismogram y=3100 m – (a), zero offset seismogram x=5100 m – (b).

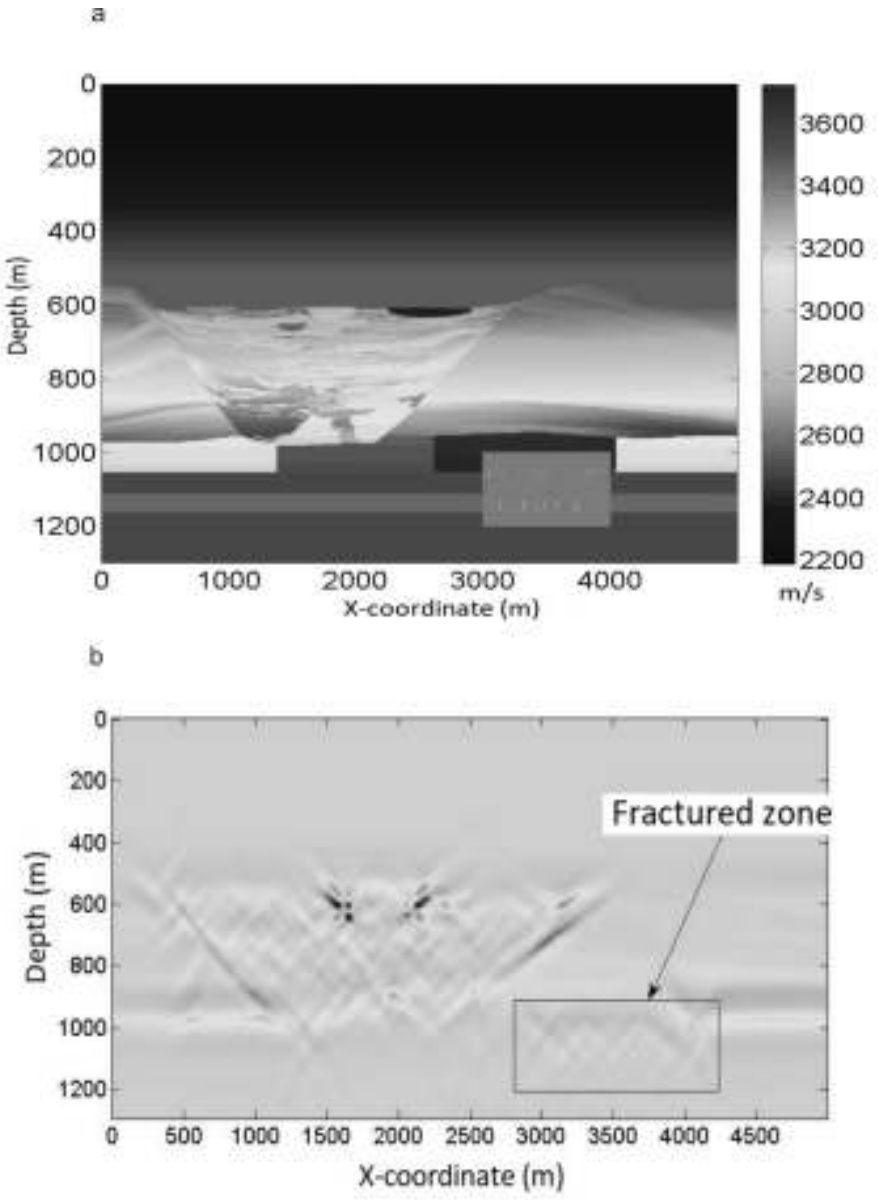

Figure 12. The vertical section y=5100: a) – model, b) – the diffraction image.

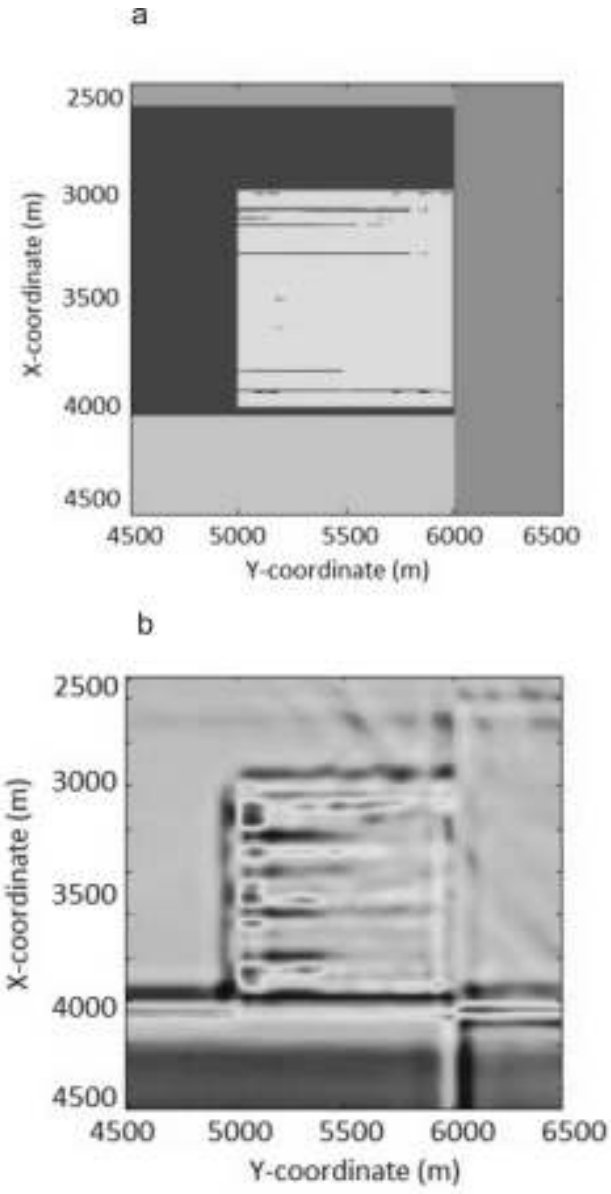

Figure 13. The horizontal section at the level of fractured zone z=1100 m: a) – model; b) – the diffraction image.

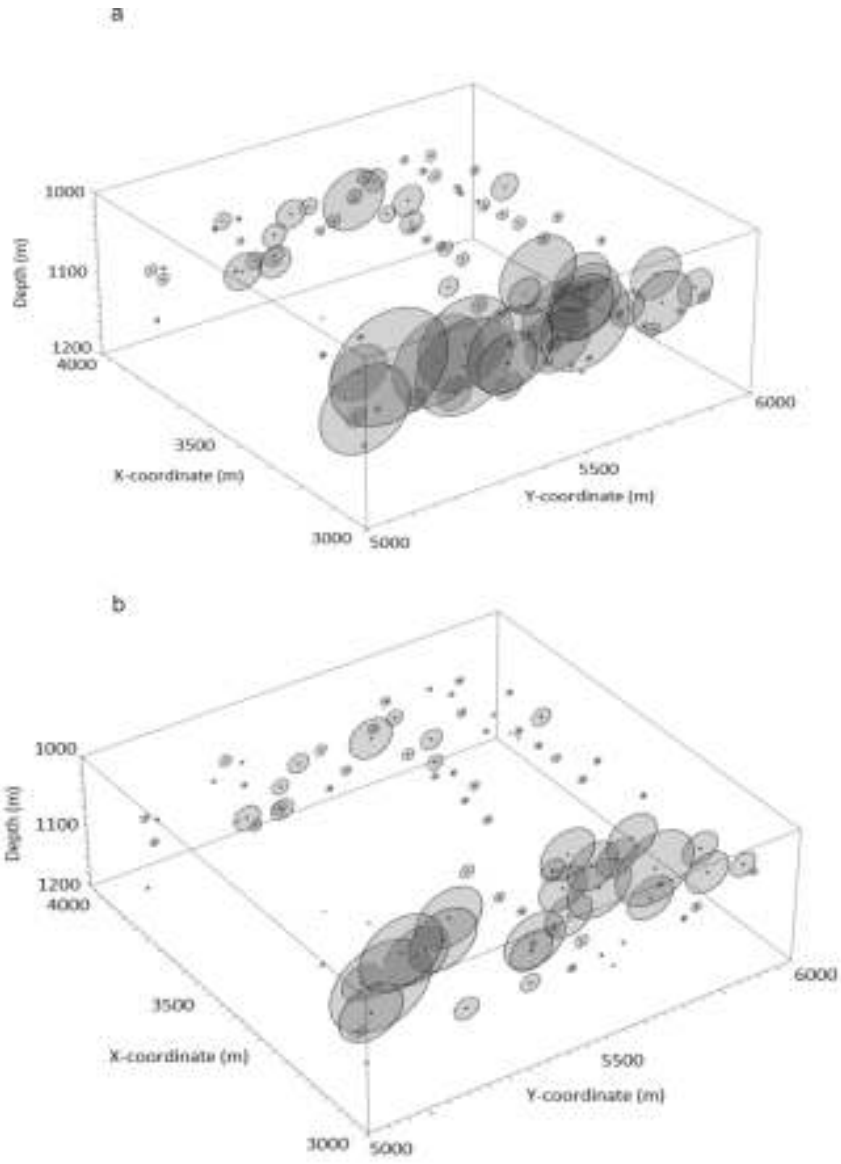

Figure 14. DFN seismic models in the XY plane (Z=1100 m): a) – reconstructed from the model; b) – recovered from the diffraction image by topological analysis.

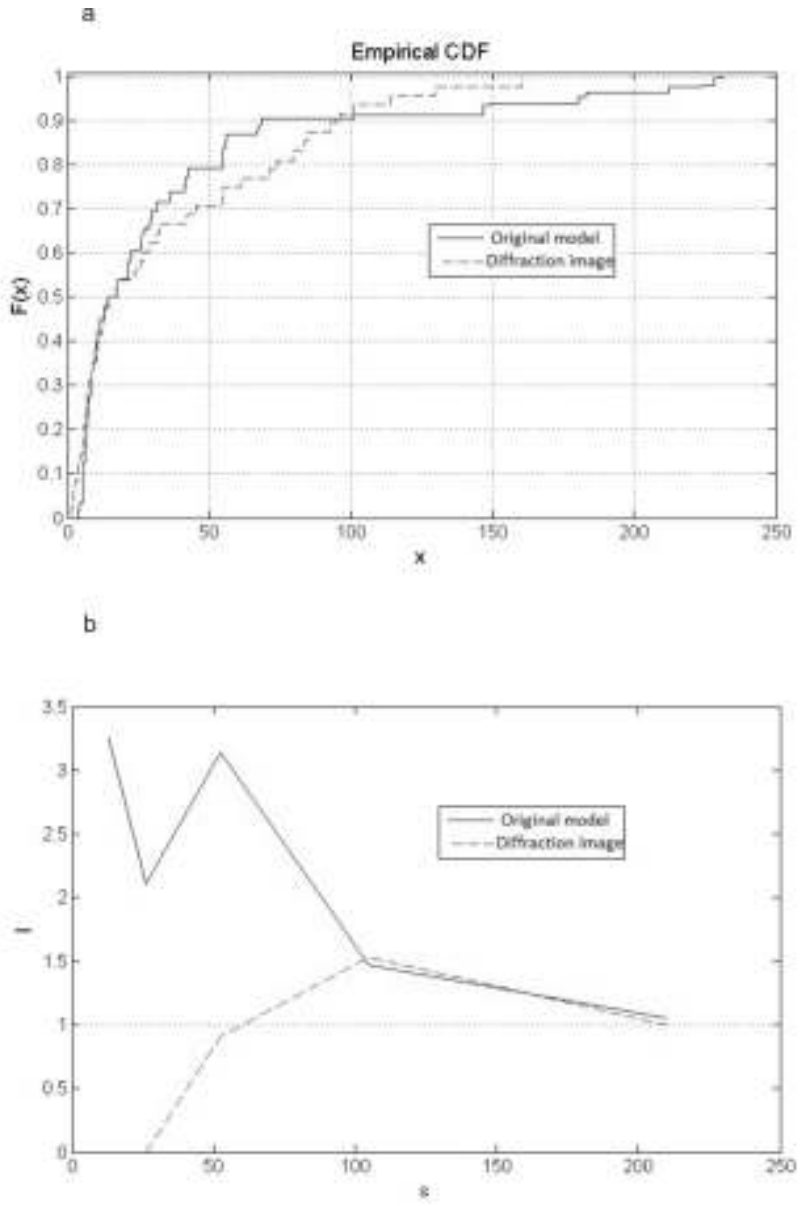

Figure 15. a) Empirical distribution functions estimated for the diffraction image and original model. b) Morisita diagrams estimated for the diffraction image and original model.

DATA AND MATERIALS AVAILABILITY

Data associated with this research are available and can be obtained by contacting the corresponding author.